

1 **Analysis of the instability conditions and failure mode of a**
2 **special type of translational landslide using long-term**
3 **monitoring data: A case study of the Wobaoshi landslide (in**
4 **Bazhong, China)**

5 Yimin Liu^{a,b}, Chenghu Wang^{a,*}, Guiyun Gao^a, Pu Wang^a, Zhengyang Hou^a, Qisong Jiao^a

6 ^a Institute of Crustal Dynamics, China Earthquake Administration, Beijing, 100085, China

7 ^b School of Manufacturing Science & Engineering, Sichuan University, Chengdu, 611730, *China*

8
9 **Abstract:** A translational landslide comprising nearly horizontal sandstone and mudstone interbed
10 was widely developed in the Ba river basin of the Qinba–Longnan mountain area. Some
11 progresses on the formation mechanism and failure mode for this type of rainfall-induced
12 landslide have been made in the previous research; however, owing to lack of landslide
13 monitoring data, it is very difficult to demonstrate and validate previously-established
14 geomechanical model. This study considered a translational landslide with an unusual morphology:
15 the Wobaoshi landslide, located in Bazhong city, China. Firstly, the engineering geological
16 conditions of this landslide were ascertained through field investigation, and the deformation and
17 failure mechanism of the plate-shaped sliding body were analyzed. Secondly, long-term
18 monitoring engineering was conducted to obtain multi-parameter monitoring data, such as crack
19 width, rainfall intensity, and pore-water pressure. Finally, based on the geomechanical model
20 analysis of the multi-stage sliding bodies, the equation for the critical water height of the
21 multi-stage plate girders, h_{cr} , was established, and the long-term monitoring data were used to
22 verify its reliability. On the basis of numerical simulation and calculations, the deformation and
23 failure modes of the plate-shaped sliding bodies were analyzed and investigated. In conclusion,

the multi-parameter monitoring data proved that the stability of the sliding body is controlled greatly by the rainfall intensity and pore-water pressure and the pore-water pressure in the crack is positive for the initiation of the plate-shaped bodies sliding, and at the same time, one optimized monitoring methodology for this type of landslide was proposed. Therefore, this research findings are of theoretical and practical significance for the intensive study of translational landslides in this area.

Keywords: Translational landslide; Long- term monitoring; Instability conditions; Failure mode; Plate-shaped sliding body; Pore-water pressure.

0. Introduction

A special type of landslide occurs in the red beds of the Qinba–Longnan mountainous area. This landslide is mainly developed in the rock mass of the nearly horizontal sand and mudstone interbed in the Ba river basin, and it has the following characteristics: the cover layer is extremely thin, generally not more than 5 m; the sliding surface is close to horizontal; and the rock layer inclination angle is generally only 3° - 8° . The sliding body of this landslide is typically a thick layer of sandstone with good integrity, and its bottom is a weak layer comprising mudstone. During monsoon, particularly when rainstorms occur, the sliding body is pushed horizontally along the sliding surface. Some scholars call this phenomenon a flat-push landslide, which is a typical rainfall-induced landslide (Zhang et al., 1994; Fausto G. et al., 2004; Xu et al., 2010).

Research on the formation mechanism and deformation mode of a translational landslide is mainly based on two perspectives. The first category includes the translational landslides is primarily induced by the hydrostatic pressure or confined water pressure resulting from rainstorms

(Kong and Chen, 1989; Matjaž et al., 2004; Yin et al., 2005). The sliding body of the thick sandstone can slide along the surface because of the hybrid action of the hydrostatic pressure in cracks and the uplift force of the sliding surface (Wang et al., 1985; Zhang et al., 1994; Xu et al., 2006; Fan, 2007). Simultaneously, the sliding soil, expanded by rain water, causes a slip between nearly horizontal layers (Yin et al., 2005). The second category includes landslides wherein the hard rock layer covered by the upper layer (such as granite and sandstone) has a crushing effect on the lower weak rock layer, thereby causing the rock mass to laterally expand, resulting in a landslide (Cruden et al., 1996; Emelyanova, 1986).

Regarding the theoretical study on rainfall-induced translational landslide, scholars worldwide have used physical simulation experiments, geomechanical model analysis, and satellite remote-sensing methods to investigate the genetic mechanism, initiation criteria, and sensitive safety factors. Fan Xuanmei et al. (2008) reproduced the deformation and failure process of landslides through physical simulation, and further verified the formation mechanism and initiation criterion formula of the flat-push landslide previously studied by Zhang et al. (1994). Sergio et al. (2006) focused on the influence of pore-water pressure on the stability of rainfall-induced landslides, and studied the soil failure mode based on pore-water pressure via simulation experiment. Mario et al. (2008) and Teixeira et al. (2015) selected rainfall data from historical periodic rainfall conditions, and used physical experiments to establish an optimization model for rainfall-induced landslide initiation criteria for landslides in the southern Apennines and shallow landslides in northern Portugal; they also evaluated landslide susceptibility and safety factors to evaluate the possibility of landslide resurrection induced by rainstorms. Barlow et al. (2003) and Martin et al. (2005) used US land satellite called enhanced thematic mapper (ETM+)

and digital elevation model (DEM) data to detect the residues of translational bedrock landslides in an alpine terrain. Bellanova et al. (2018) used resistivity imaging to investigate the Montaguto translational landslide in the southern part of the Apennines; they also established a refined geometric model to observe the lithologic boundaries, structural features, and lateral and longitudinal discontinuities associated with sliding surfaces.

Through data collation and analysis of the current research status of translational landslides, scholars worldwide have conducted further research on the formation characteristics and genetic mechanism of translational landslides. Based on the results of previous studies, the main focus of this study is on the following two aspects.

(1) The occurrence of plate-shaped translational landslides is often unexpected and covert. Plate-shaped translational landslides are primarily induced by rainfall; such events often occur in the red-bed zone of the Qinba–Longnan mountainous area. Due to the dense population and infrastructures in this area, plate-shaped landslides, characterized by large volumes, and covert and abrupt occurrence, often cause massive property loss and casualties. In the previous field investigation, such destructive events are often classified as small-scale rock mass collapses; hence, the dangers posed by such kind of landslides were easily ignored.

(2) The field investigation and monitoring data for this kind of landslide is often absent. In the past research, specific geomechanical and physical models have been established using historical rainfall records, and laboratory physical experiments have been conducted in the to verify the failure model. However, long-term on-site monitoring data and related analysis and findings for such landslides have not been reported in publications according to literature review. Therefore, several key field monitoring parameters, such as width of rear crack, real-time rainfall,

pore-water pressure, and groundwater level, should be obtained to investigate and validate the deformation and failure mode of translational landslides, and be utilized to establish a geomechanical model.

Based on the formation mechanism of the translational landslide established by previous studies, research chosen a typical and specific translational landslide (the Wobaoshi landslide) in the Ba River Basin of the Qinba–Longnan mountainous area, and conducted field investigation, long-term (February 2015 to July 2018) monitoring, geomechanical model analysis, and numerical simulation to investigate the instability conditions and variation failure modes of this translational landslide under the influence of periodic rainfalls.

1. Engineering Geology Characteristics of the Wobaoshi Landslide

1.1. Field Survey of the Landslide

The Wobaoshi landslide is located in the Ba river basin in the Qinba–Longnan mountainous area. Its specific location is in Baiyanwan village, Sanhui town, Enyang district in Bazhong, China. Fig. 1 presents its geographical location and elevation information. The Wobaoshi landslide is located on the left bank of the Shilong river. The front edge of this landslide is in the curved section of the river, and its left boundary gully is located on the concave bank on the river's left bank. The landslide area is classified as a red-bed layer in a low mountainous area, the vegetation of its sliding body is dense, and its geomorphic unit is cuesta structural slope. The geological structure of the landslide body lies on in the south side of the Nanyangchang anticline, and its stratum is the mudstone and sandstone interbed of the Penglaizhen Formation of the upper Jurassic series (Chen et al., 2015).

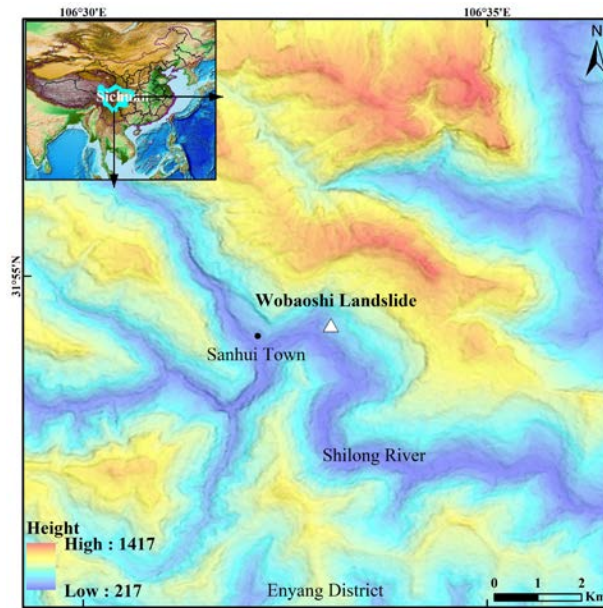


Fig. 1 Geographical location and elevation map of the Wobaoshi landslide.

This landslide is common in the eastern subtropical monsoon climate region, where rainfall is abundant and mostly concentrated from May to October, accounting for 75% - 85% of the total annual rainfall. The monthly average rainfall is above 100 mm, of which the highest occurs in July, the monthly average rainfall in July is over 200 mm and often accompanied by rainstorms, and the rainfall gradually decreases after August in this region (Chen et al., 2015). The types of groundwater are mainly fissure water in weathered bedrock and pore-water in trailing edge cracks, and the dynamic change of groundwater is considerably affected by climatic change.

1.2. Landslide Characteristics and Forming Conditions

1.2.1 Engineering Geology Characteristics

According to the satellite remote-sensing interpretation and landslide survey, the shape of the sliding body is a flat long rectangle on the plane. Its longitudinal (sliding) direction is nearly 32 m, the lateral width is 160 m, the average thickness of the sliding body is approximately 30 m, and its volume is approximately $1.536 \times 10^5 \text{ m}^3$. This sliding body belongs to small- to medium-sized landslides according to the typical scale. The sliding direction of the landslide is 249° , and the overall attitude of the rockbed is $170^\circ - 180^\circ \angle 6^\circ - 8^\circ$. The strike in this landslide is nearly parallel to the overall trend of the bank slope, which is a typical nearly horizontal consequent bedding rock slope. Fig.2 shows a planar graph of the Wobaoshi landslide and photographs of five observation points. Fig. 3 presents I-I' sectional graph of the landslide.

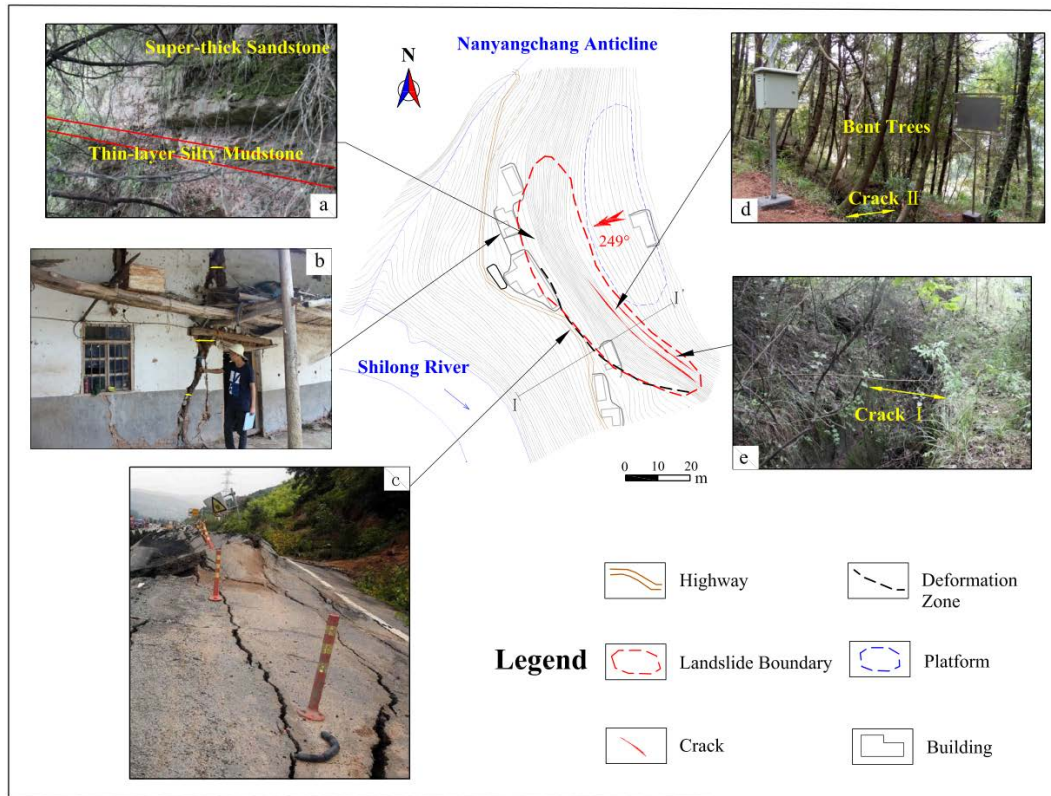


Fig. 2 Topographic map of the Wobaoshi landslide and photographs of observation points: (a) exposed bedrock at the front edge; (b) the houses had cracked at the front edge (c) the roadbed is pushed uplifted at the front edge; (d) crack II and bent trees; and (e) crack I.

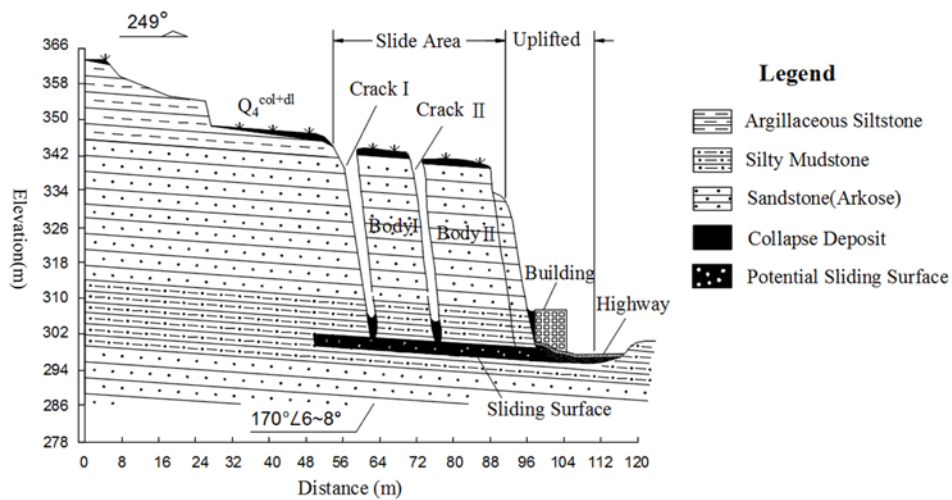


Fig. 3 I-I' sectional graph of the landslide

As shown in Fig. 2, the landslide shape is special, the longitudinal length is much less than the lateral width and is even smaller than the thickness of the sliding body. Therefore, this body can be easily mistaken for a multistage dangerous rock mass with dumping deformation during disaster investigation. According to Fig. 3, the inclination of the landslide is almost erect, and a

group of long and straight structural planes parallel to the slope cut the slope into two thin plates (sliding bodies I and II); furthermore, the surface structure of the slope has a certain degree of aperture, both sides of the crack are closed, and the bottom of the crack is filled with clay in addition to gravel and collapse deposits.

1.2.2 Forming Conditions

The sliding body of the Wobaoshi landslide formed two obvious cracks from the outside to the inside, which cut and disintegrated the sliding body into plate-shaped blocks from front to back, as shown in the photographs of observation points c and d in Fig. 2. Then, the plate-shaped sliding bodies I and II were formed. The landslide is a two-stage translational landslide in which the longitudinal length of sliding body I is 12 m, the identifiable lateral width is ~ 70 m and the thickness is ~ 30 m, the longitudinal length of the sliding body II is 16 m, the identifiable lateral width is ~ 65 m, and the thickness is ~ 28 m. Sliding body I forms crack I with the trailing edge of the landslide, and sliding body II forms crack II with sliding body I. When large rainfall intensity occurs during monsoon, the pore-water in the cracks can be observed, thus indicating that cracks I and II have preferable water-storage conditions.

As the photograph of observation point d in Fig. 2 shows, bent trees grow on the trailing edge of landslide bodies I and II. The trees on the landslide are skewed with the soil mass sliding, and after the sliding stops, the upper part of the trunk turns to the upright state year by year. The existence of bent trees represents the tendency of the slope body to become unstable or the existing landslide accumulation body tends to slide again, this is also historical evidence of the slow sliding of the landslide (Zhang Lizhan et al., 2015).

As the photo of observation point a in Fig. 2 shows, the shallow surface of the Wobaoshi landslide is a 2–3 m thick layer of collapsed and plowed soil. The sliding body contains extremely thick sandstone with good integrity, and the bottom sliding surface is a weak interlayer comprising of silty mudstone. In summary, the Wobaoshi landslide is a typical and special translational landslide, and based on the characteristics of its plate-shaped body, it can be considered a plate-shaped landslide (Fan et al., 2008; Xu et al., 2009).

The engineering geological conditions of the Wobaoshi landslide are inferred on the basis of its characteristics; i.e., the rapid immersion of groundwater softens the joint surface of soil and

rock formation, especially under a rainstorm. Then, the group of open cracks parallel to the slope in the sliding body is concentrated and quickly filled with water, following which groundwater level rises and the pore-water pressure increases sharply, such that the sliding bodies I and II slide horizontally along the contact surface of the bottom sand-mud-rock weak layer. This condition changes the stress mode and equilibrium state of the rock and soil mass, thereby easily inducing a landslide. As shown observation point b and c in Fig. 2, the Wobaoshi landslide seriously threaten residential houses and highways, the houses had cracked and highways had uplifted on its front edge, so this landslides seriously threatens the safety of people's property and transportation.

2. Landslide Monitoring Scheme and Monitoring Data Analysis

2.1. Long-term Monitoring Scheme

According to the detailed investigation of the Wobaoshi landslide, two cracks extend through the sliding surface at the trailing edge of the landslide, and the pore-water in the cracks exists during periodic rainfalls. As the hydrostatic pressure in the cracks strongly influences the stability of the plate-shaped landslide (Fan Xuanmei et al., 2008; Guo Xiaoguang et al., 2013), via real-time monitoring of cracks, rainfall and pore-water pressure measurements were conducted from February 2015 to July 2018 to determine the landslide state in different periods such as rainy and non-rainy seasons, together with the interaction between multilevel plate girders and sliding surface. Fig.4 shows the layout graph of the monitoring equipment.

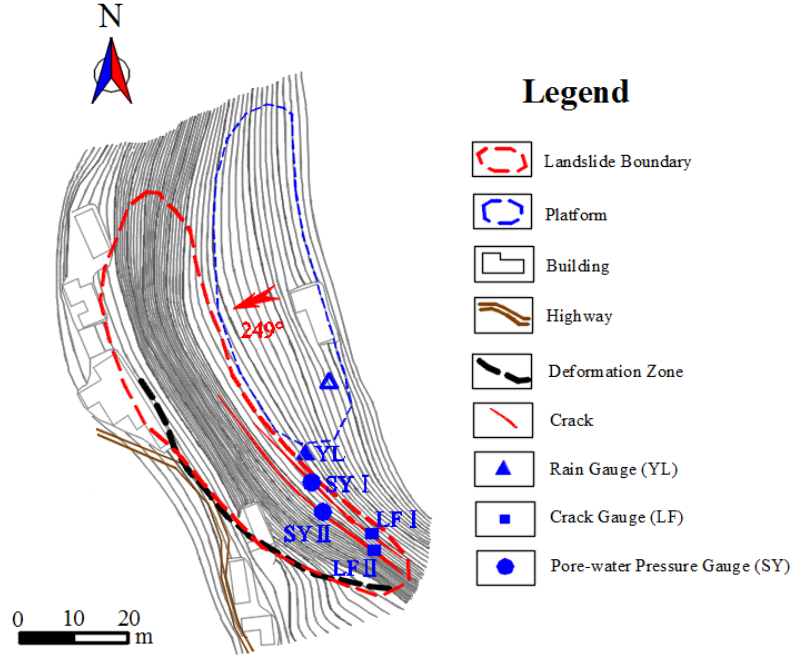


Fig. 4 Layout planar graph of the monitoring equipment

As shown in Fig. 4 shows, two non-contact crack automatic monitors, LF I and II, are installed on both sides of cracks I and II, respectively, to record real-time variation of the width of the two cracks (Yimin Liu et al., 2015). An automatic rain gauge is installed in flat space and no tree occlusion is observed at the trailing edge of the landslide to record real-time and cumulative values of the rainfall. Two pore-water pressure gauges are installed at the bottom of crack I and II to measure the pore-water pressure. The value of pore-water level, h_c , can be calculated using the relation $h_c = H - h_i + h_s$, where h_i is the installation depth of the pore-water pressure gauge; H is the depth of the crack; and h_m is the measured value of the pore-water pressure gauge.

In this example, the initial width value of crack I is 5.640 m, and the initial width value of crack II is 4.492 m (the first measurement was conducted in January 2015); the installation depth $h_{i1} = 24.72$ m, and the depth of crack I is $H_1 = 38$ m, with $h_{c1} = 13.28\text{m} + h_{m1}$. Additionally, the installation depth $h_{i2} = 24.85$ m, and the depth of crack I is $H_2 = 35$ m, and $h_{c2} = 10.15\text{m} + h_{m2}$. The monitoring frequency of the crack width is thrice a day, the monitoring frequency of the pore-water pressure is twice a day, and the rainfall intensity adopts the accumulative value of one month. The multiparameter monitoring data are transmitted to the monitoring server through the GPRS network.

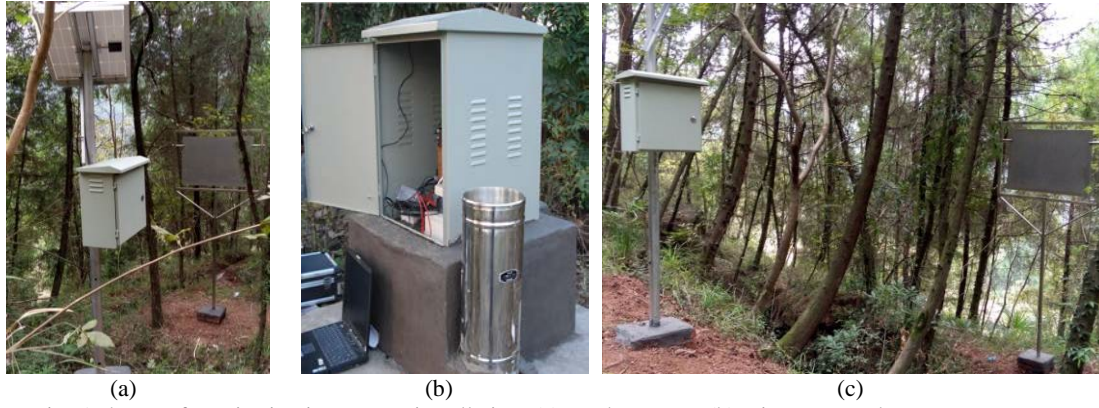


Fig. 5 Photos of monitoring instrument installation: (a) crack I gauge; (b) rain gauge and pore-water pressure gauge; (c) crack II gauge.

2.2. Monitoring Data Analysis

By the monitoring work performed on the Wobaoshi landslide for three-and-a-half years (February 2015 to July 2018), this study selected the typical data of the width of cracks I and II, the pore-water pressure and the rainfall intensity, details of these monitoring data are in listed in Tables 1 and 2. The corresponding time curves in Fig.6 show the monitoring data of the rainfall intensity and the width of cracks I and II. Fig.7(a) and 7(b) present comparison curves of the monitoring width data of cracks I and II against their pore-water pressures, respectively.

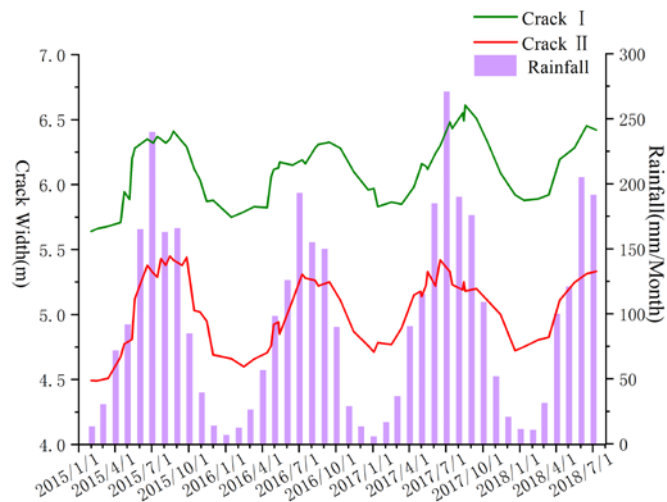


Fig. 6 Monitoring data curves (rainfall intensity and width of cracks I and II)

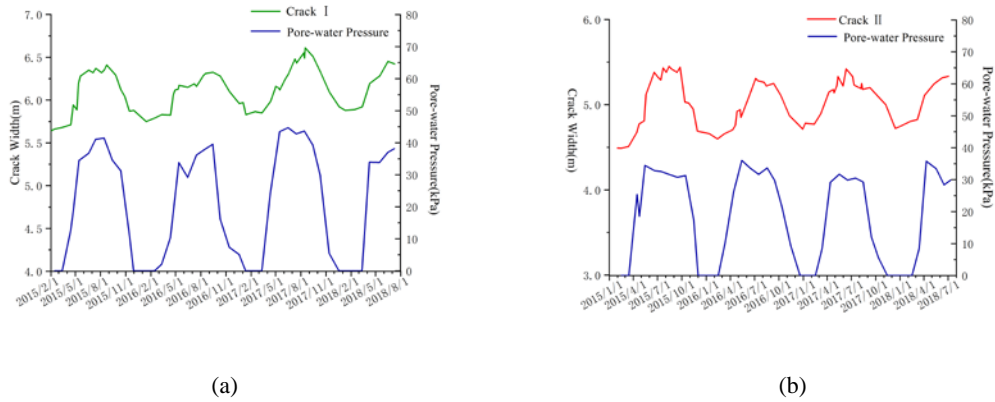


Fig. 7 Monitoring data curves: (a) width of crack I and its pore-water pressure; (b) width of crack II and its pore-water pressure.

Based on the comprehensive comparison and analysis of the data curves presented in Figs. 6 and 7, this study concludes that the Wobaoshi landslide is still in creep deformation state, and the plate-shaped sliding body exhibits a regular trend with changes in rainfall intensity and pore-water pressure. Cracks I and II show a preferable water-storage capacity during monsoon, and increasing pore-water pressure affects the crack width variation. The specific analysis is as follows.

(1) A clear correspondence exists between the absolute amount of crack width change and season change (i.e. change in rainfall intensity); the magnitude of the rainfall intensity determines the change of the width of the two cracks. As shown in Fig. 6, the widths of cracks I and II widen as the rainfall intensity increases during monsoon (May to September), and their crack widths gradually decrease as the rainfall intensity lowers during the non-rainy seasons (October to April in the next year). As indicated in Fig. 8, the maximum width of crack I reaches 6.615 m, and the absolute stretching amount of this crack is close to 1 m in the July–August period in 2017 (monthly rainfall exceeding 250 mm). The maximum width of crack II is also in the range of 5.40–5.45 m, and its absolute stretching amount exceeded 1 m during July–August 2015 and

July–August 2017. During non-rainy seasons, when the rainfall intensity lowers, the crack width begins shrinking, and it decreases to its minimum in January in each monitored year.

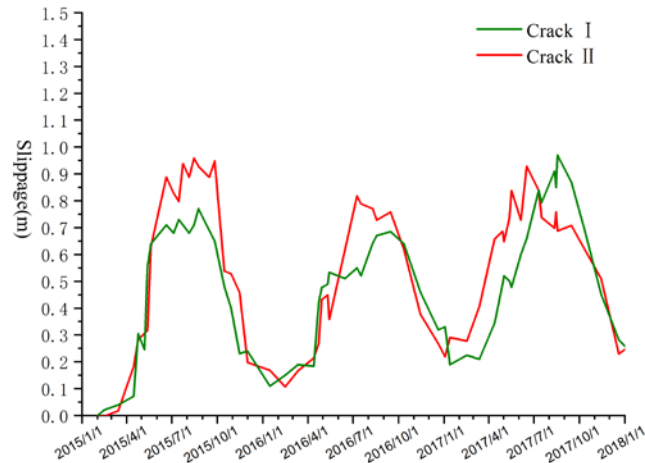


Fig. 8 Absolute slippage amount curves of crack I and II

(2) The width of cracks I and II tend to increase year by year, indicating that the two-stage sliding body of the Wobaoshi landslide is still moving along the sliding surface because of the influence of rainfall. In Fig. 6, the measured data in the monitoring period indicate that the minimum widths of crack I and II are gradually increasing, and their maximum value is considerably affected by the rainfall intensity of a particular month.

(3) Fig.7 shows that the stretching of cracks I and II, or both follows the same trend as the pore-water pressure, i.e., the magnitude of pore-water pressure determines the width variation of the cracks. Fig.7 also shows that the water-storage capacity of crack I is good during monsoon, and after the sliding body slides, it can maintain a certain pore-water level because of rainfall replenishment. Additionally, the increase in rainfall intensity increases the water level in the cracks, and the increase in pore-water pressure positively affects the initiation of the plate girder.

The curve in Fig. 8 shows that the increase in pore-water pressure has a significant causal relationship with the stretching of the cracks.

3. Model Calculation and Numerical Simulation

To construct a generic model of the evolution process of the Wobaoshi landslide, a geomechanical model of plate-shaped sliding bodies was established, its stability was calculated, and it was combined with monitoring data for a comparative analysis. According to previous findings(Fan, 2007; Fan et al., 2008; Xu et al., 2010), when many penetrating cracks are parallel to the slope in the rock mass, and these cracks are filled with water, the water pressure on both sides of each plate-shaped body attains in a balanced state except for the outermost body. However, once the outer body slides, owing to the sudden decrease of the pore-water level in the trailing edge crack, the water pressure around immediately following plate-shaped body becomes unbalanced, and new sliding damage is induced (Fan, 2007; Xu, 2008).

3.1. Model Establishment and Stability Calculation

According to characteristics of the Wobaoshi landslide in Section 1.2, when the geomechanical model is established, the cover layer is neglected, and the static geomechanical model of the plate-shaped rock sliding body is established based on the limit equilibrium method. The basic characteristic of the limit equilibrium method is that the Mohr-Coulomb failure criterion of the soil in static equilibrium conditions is considered, that is, the problem's solution is solved by analyzing the destruction of the soil's balance. And soli elastic-perfectly plastic model was chosen, which obey the Mohr-Coulomb failure criterion and associated flow rules (Darve et al., 2004; Labuz et al., 2015).

For the failure mode of the two-stage plate girders of the Wobaoshi landslide, this study selected a typical section of plate-shaped sliding bodies and established the geomechanical model, shown in Fig. 9. In this section, first, a stability analysis of the outer layer plate girder II, is conducted and then the inner plate girder I is analyzed.

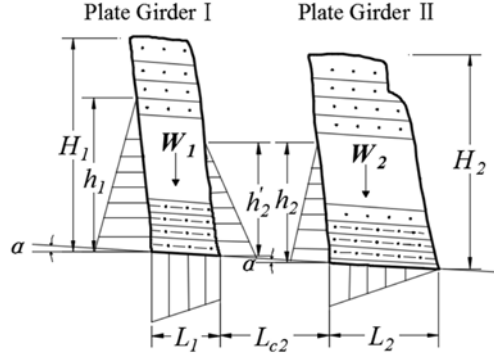


Fig. 9 Geomechanical model of two-stage plate-shaped sliding bodies

In Fig. 9, α is the angle of the sliding surface, h_1 and h_2 are the heights of the pore-water levels in cracks I and II, respectively; L_1 and L_2 are the widths of plate girders I and II, respectively; L_{c2} is the distance between plate girder I and II; H_1 and H_2 are the heights of plate girders I and II; respectively, and W_1 and W_2 are the self-weights of plate girders I and II per unit width, respectively. According to the relationship between the stability coefficient of plate girder, K , and the height of the pore-water level, h , shown in Fig. 8 (Zhang et al., 1994; Xu et al., 2010), while considering the internal cohesive force of the sliding surface, the equation to calculate the stability coefficient, K_2 , of the outer layer plate girder II is expressed as follows:

$$K_2 = \frac{\left(W_2 \cos \alpha - \frac{1}{2} \gamma_w h_2 L_2 - \frac{1}{2} \gamma_w h_2^2 \sin \alpha \right) \tan \theta + c L_2}{\frac{1}{2} \gamma_w h_2^2 \cos \alpha + W_2 \sin \alpha} \quad (1)$$

In Eq. (1), c is the internal cohesion of the sliding surface; γ_r is the saturated gravity of the sandstone; γ_w is the gravity of water; and $W = H \cdot L \cdot \gamma_r$. K_2 is set to 1, i.e., the plate girder II is set in a critical sliding state (GB/T 32864-2016, 2017). Then Eq. (2) of the maximum pore-water level of plate girder II, h_{cr2} , is derived from Eq. (1).

$$h_{cr2} \approx \frac{1}{2 \cos \alpha} \left[L_2^2 \tan^2 \theta + \frac{8}{\gamma_w} (W_2 \cos \alpha \tan \theta - W_2 \sin \alpha + cL_2) \cos \alpha \right]^{\frac{1}{2}} - \frac{L_2}{2 \cos \alpha} \tan \theta \quad (2)$$

According to the experimental data of the triaxial confining pressure of the Wobaoshi landslide's rock core (Chen et al., 2015), the internal friction angle of the sliding surface is $\theta = 11.2^\circ$, the saturated gravity of the sandstone is $\gamma_r = 19.2 \text{ kN/m}^3$, the gravity of clear water is $\gamma_w = 9.8 \text{ kN/m}^3$, and the internal cohesion of the sliding surface is $c = 10.2 \text{ kPa}$. According to the sectional graph of the Wobaoshi landslide (see Fig. 2), $H = 35 \text{ m}$, $L = 16 \text{ m}$, and $\alpha = 6^\circ$. Therefore, according to Eq. (2), $h_{cr2} = 13.896 \text{ m}$.

Based on the stability analysis of plate girder II, combined with Eq. (1), Eq. (2), and Fig. 7, the equation to calculate the stability coefficient K_I of the inner layer plate girder I can be expressed as Eq. (3). In addition, $h_2' = h_2 - L_{c2} \sin \alpha$ and $L_{c2} = 3.8 \text{ m}$; therefore, $h_2' = 13.499 \text{ m}$.

$$K_I = \frac{\left[W_1 \cos \alpha - \frac{1}{2} \gamma_w (h_1 + h_2') L_1 - \frac{1}{2} \gamma_w (h_1^2 - h_2'^2) \sin \alpha \right] \tan \theta + cL_1}{\frac{1}{2} \gamma_w (h_1^2 - h_2'^2) \cos \alpha + W_1 \sin \alpha} \quad (3)$$

Similarly, K_I is set to 1 and, in plate girder I, $H_I = 38 \text{ m}$, $L_I = 12 \text{ m}$, $\alpha = 6^\circ$, $h_2' = 13.499 \text{ m}$, therefore, the maximum pore-water level h_{cr1} of plate girder I can be calculated using the Eq. (3) and $h_{cr1} = 17.249 \text{ m}$.

The preceding calculation results show that, when the pore-water level at the trailing edge of the plate girder reaches the maximum height at which the landslide begins, i.e., when $h_{cr1} = 17.249 \text{ m}$ and $h_{cr2} = 13.896 \text{ m}$, the pore-water pressure triggers the plate-shaped sliding bodies. In next section, the pore-water monitoring data, which were acquired via the landslide monitoring are

used to verify the equation.

The pore-water monitoring data in Section 2.2, which were acquired via the landslide monitoring engineering, were used to test the equation for calculating the maximum height of multistage plate girders, h_{cr} . According to the monitoring data of the pore-water pressure and the installation depth of the sensors, the actual calculated maximum height values h_{c1} and h_{c2} of the pore-water level are presented in attached Table 3. Combined with the change in the absolute stretching amount in Fig. 8, typical data of the measured pore-water level are selected, corresponding to the sudden change in the absolute slippage (see Table 3 for details), as shown in Fig.10.

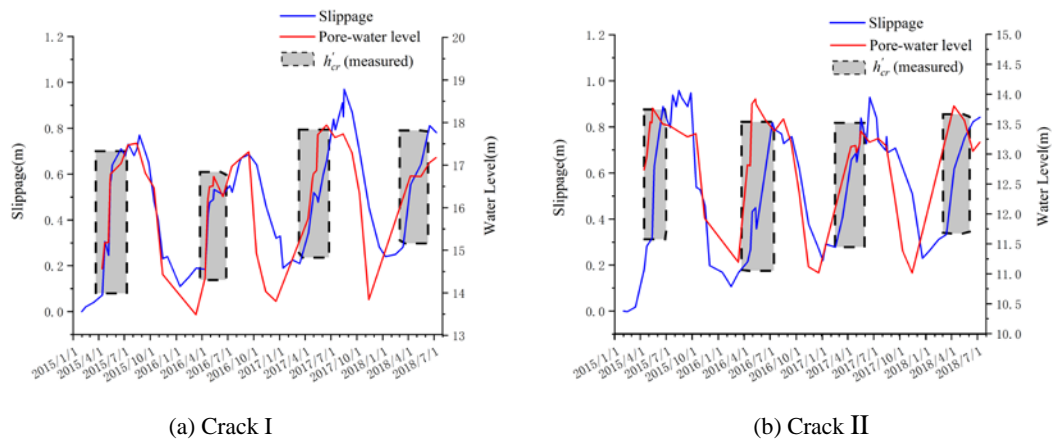
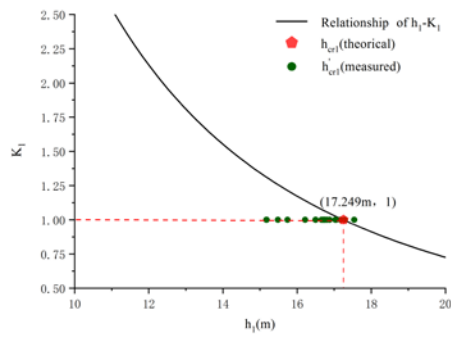
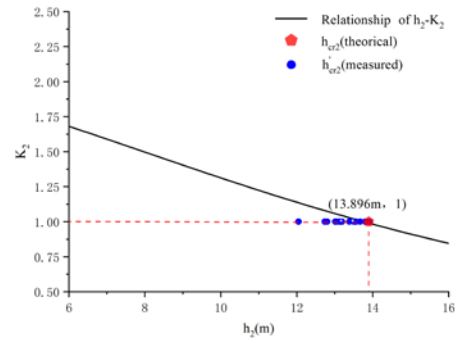


Fig. 10 Determination of the maximum measured pore-water level h_{cr}

The dotted boxes in Fig. 10 represent the value of the pore-water level when the bodies are sliding, i.e., the maximum pore-water level, h_{cr} , which causes the sliding body to be unstable. The measured h_{cr} in Fig. 10 can be compared to the relationship between the pore-water level, h , and the stability coefficient of the plate girder, K , in equation (1) and (3), which are also shown in Fig. 10.



(a) Crack I



(b) Crack II

Fig. 11 Comparison of h_{cr} (measured) and h_{cr} (theoretical)

In Fig. 11, the curves of the h - k relationship represent equations (1) and (3). The frequency of h_{cr} (measured) in Fig. 11 shows that most of the monitoring pore-water levels are not higher than those theoretically calculated. The Wobaoshi landslide monitoring example shows that in most cases, when h_{cr} (measured) $\leq h_{cr}$ (theoretical), the pore-water pressure causes the instability of the sliding body.

3.2. Numerical Simulation of the Plate-shaped Sliding Bodies

The numerical simulations and calculations of the plate girder were performed using MIDAS GTS NX geotechnical finite element software. First, the 1:1 sliding body model in Fig. 9 was introduced into the finite element software, and the mechanical parameters of the sliding body model, i.e., elastic modulus, Poisson's ratio, gravity internal cohesion and friction angel, were defined as shown in Table 4. The position of the right side of the landslide about 30m from the foot of the slope is selected as the right boundary of the model; the lower boundary is setted at the elevation of 0 m; the left boundary is located inside the mountain, about 30m away from the plate girder I. The element type adopts a plane strain quadrilateral-triangle mixing element, and the whole model is divided into 13775 elements and 14026 nodes. Here we constrain the vertical and horizontal displacement of its bottom boundary, and the left and right boundary conditions are set

to constrain the horizontal displacement. The model uses steady-state seepage calculation, and the water levels at the left and right boundaries were set to 342 and 275 m, respectively. The boundary conditions are set as follows.

(1) For the displacement boundary, the left and right boundaries constrained the displacement in the X-direction; i.e., $T_x = 0$. For the bottom boundary, the displacement in the X and Y directions was constrained; i.e., $T_x = T_y = 0$.

(2) For the seepage conditions, the water levels at the left and right boundaries were set to 342 and 275 m, respectively.

The typical pore-water-level data in the crack I and crack II presented in Table 3 were introduced into the finite element model, and were selected for a typical change period presented in Table 5, followed by numerical calculations to obtain the typical deformation and displacement states of plate-shaped sliding bodies in the rainy and non-rainy seasons, as shown in Fig. 12.

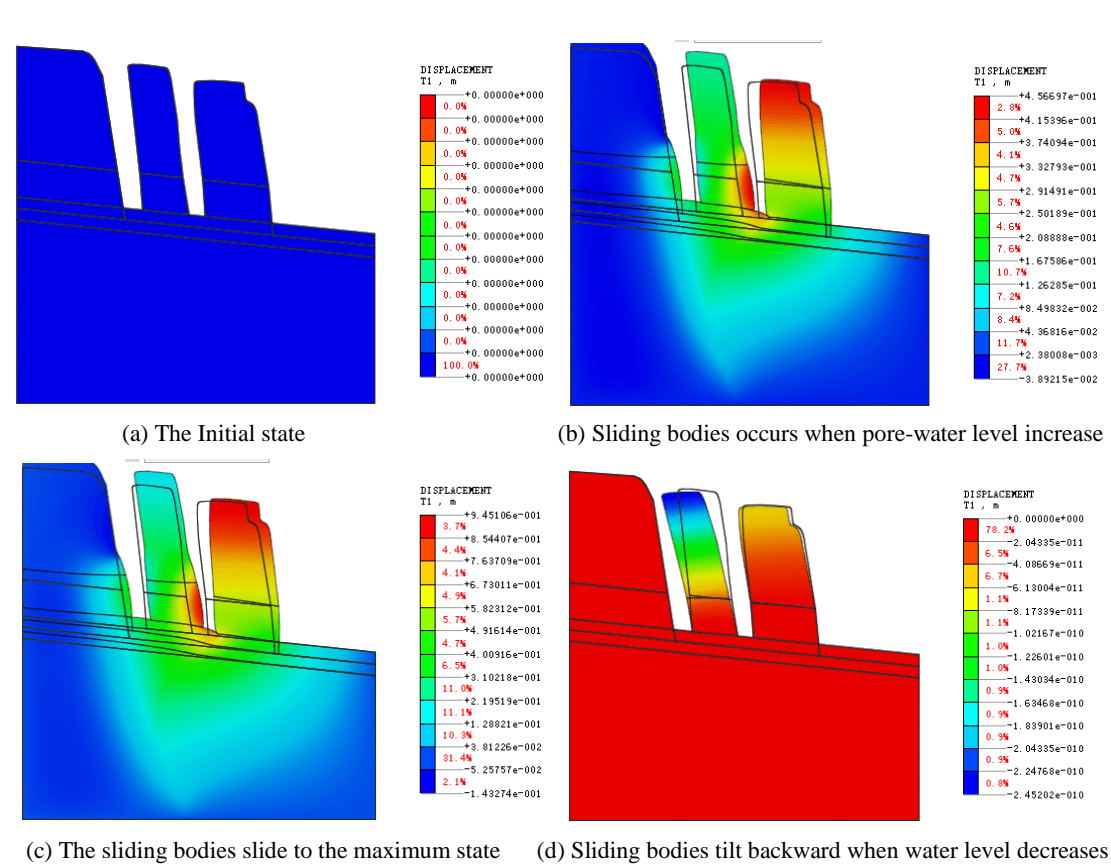


Fig. 12 Example of finite element simulation and numerical calculation

The initial displacement state in Fig. 12(a) is set to zero for the following analysis. Figure

12(b) shows that, under the combined effect of the pore-water pressure and seepage, the multistage plate girders slide horizontally along the sliding surface. In Fig. 12(c), the multistage plate girders have slid to the maximum distance, where the maximum distance of slider II is 0.945 m, which is close to the value obtained in the monitoring data. In Fig. 12(d), owing to the decrease in pore-water level in the non-rainy season, sliding bodies I and II have the same tendency to tilt backward. Therefore, the calculation results of the numerical simulation can corroborate the sliding-body mechanics model and the landslide monitoring data.

4. Discussion

As mentioned in the previous sections, this special type of translational landslide, which has a plate-shaped sliding body and is generally formed in an extremely thick sandstone slope with a thin cover layer, is nearly horizontal and has good integrity. According to the traditional theory of granular equilibrium limit, deformation or sliding movement of this nearly horizontal bedrock slope is nearly impossible, and the likelihood of forming a landslide is minimal. However, this special structure of translational landslide widely occurs in the Qinba–Longnan mountainous area during the investigation of geological hazard hidden dangers. Therefore, in the investigation and risk assessment of geological hazards, the characteristics of the plate-shaped landslide and the deformation and failure mode should be combined to detect the hidden dangers with the geological conditions of the landslide. Combining the results of previous studies with those of the monitoring, the discussion herein is divided in the following three parts.

4.1. Deformation and Failure Mode Exploration of the Wobaoshi Landslide

The monitoring results of the Wobaoshi landslide in this case validate the rainfall-triggered failure mode of the translational landslide (Zhang Zhuoyuan et al., 1994). According to the landslide monitoring data, particularly the change trend of the cracks opening and closing in Section 2.2, and the numerical simulations of the plate-shaped sliding bodies in Section 3.2, the

deformation and failure mode of the landslide were obtained, as shown in Fig. 13. Fig. 13 shows the deformation of the plate-shaped sliding bodies in the Wobaoshi landslide during the monitoring period (non-rainy season–rainy season–non-rainy season). As shown in Fig. 13(b), the large amount of rainfall in monsoon causes the cracks to be filled with water; when the pore-water level reaches the maximum height at which the landslide begins, the increased pore-water pressure positively affects the initiation of the plate-shaped sliding body (Fan Xuanmei et al., 2007). When the pore-water pressure rises to the threshold value, the plate-shaped landslide can be triggered. In this monitoring case, the pore-water pressure can push the plate-shaped sliding body by nearly 1 m, resulting in the uplift of residential houses and highways on its leading edge. Therefore, we can infer that one or more penetrating cracks are likely parallel to the slope in the landslide body. With the approach of the rainy season, the plate-shaped sliding body II begins to slide first and the water pressure balance in the cracks is destabilized. This condition causes the gliding of the plate-shaped sliding body I, thus forming a multistage translational landslide with characteristic step-by-step backward movement.

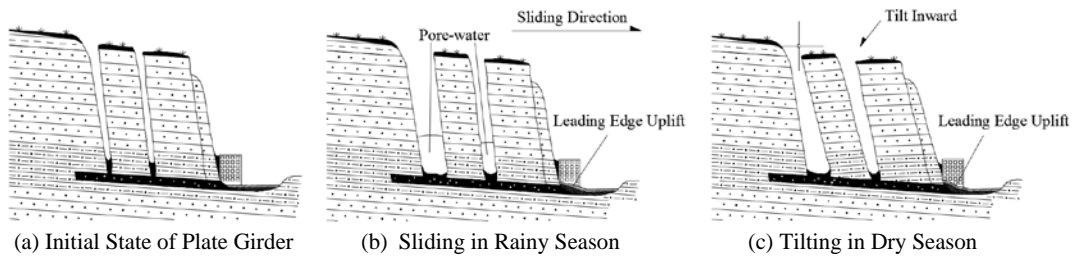


Fig. 13 Schematic of the deformation and failure mode of the Wobaoshi landslide

As shown in Fig. 13(c), the plate girder is tilted to the trailing edge by the lower pore-water level and its own weight with less rain during the non-rainy season, thereby causing the plate girder to fall backward (inside the slope) until the top of the plate girder is in contact with the slope surface, the crack width begins shrinking, and a narrow A-shaped crack is formed. Monitoring data of the Wobaoshi landslide and numerical simulation of plate-shaped sliding body also verify the deformation and failure mode of the plate-shaped landslide post landslide occurrence (Xu et al., 2010). Year after year, the cracks at the bottom of the slab-shaped sliding body grow larger, and the degree of inclination of the plate girder continues to increase. The

degree of arching of the front edge also increases, which causes the stability of the landslide to decrease continuously, thereby posing a high risk for the houses and roads on the front edge of the landslide.

4.2. Determination of Maximum Pore-water Level h_{cr}

The theoretical analysis and stability calculation of the geomechanical model of the plate girder is described in Section 4.1, together with the initiation criterion for multistage sliding bodies of translational landslide, i.e., determination of the maximum water height in the crack, h_{cr} , (Zhang et al., 1994) and calculation of the sliding body's stability coefficient, K , (Xu et al., 2010), which is determined by the theoretical calculation of strata inclination, shape, weight, and physical properties (such as saturated gravity, γ_r , internal cohesion of the sliding surface, c , and internal friction angle of the sliding surface, θ) based on the limit equilibrium theory (Lin et al., 2010). Therefore, the stability coefficient of the landslide exponentially decreases with the increase in the water-filling height of the trailing edge crack (Fan, 2008; Xu et al., 2010).

The internal friction angle, $\theta = 11.2^\circ$, is so low for clay, which seems unrealistic. However, the angle θ is obtained by triaxial compression tests of the core, which is taken from the sand-mudstone contact surface in sliding surface, and the internal friction angle $\theta = 11.2^\circ$ (Chen et al., 2015). One of the reasons may be that the clay layer is severely weathered, so its internal friction angle is small. In general, the dilatancy effect obtained by the associated flow law is much larger than the actual observation, especially in the case of lateral infinite (Tschuchnigg et al., 2015a). However, for slope stability analysis, lateral infinite is not considered in most cases, and the dilatancy effect is not significant (Griffiths & Lane, 1999). Therefore, it is reasonable to set the dilatancy angle to be equal to the internal friction angle.

In this case, in the equation for calculating the maximum pore-water level, h_{cr} , deduced in Section 3.1, comparing the measured data of the Wobaoshi landslide in Section 2.2, we can observe that the measured maximum pore-water level, h'_{cr} , is close to the theoretical maximum pore-water level, h_{cr} , thus validating the calculation equation of h_{cr} , and the instability conditions of the sliding bodies. Additionally, the most measured data in Tab. 3 are slightly smaller than the

theoretical calculation value, i.e., $h_{cr}' \leq h_{cr}$. Thus, compared with the calculation equation of the maximum water height proposed by Zhang et al. (1994) and the physical simulation experiment conducted by Fan et al. (2008), the monitoring case of the Wobaoshi landslide shows that the measured data h_{cr}' is mostly lower than the theoretical calculated value, h_{cr} , which can cause instability of the sliding body. The reason for this instability may be that the actual cohesion value c' of the sand-shale contact surface is smaller than the cohesive force value c of the sliding surface in equation (2) during the creep state of the landslide for a long duration or that the frictional angle of the sliding surface, θ , changes slightly. According to the calculation of the stability coefficient, K , in equation (2), when $c' \leq c$, $h_{cr}' \leq h_{cr}$ is obtained, the plate girder slides in the case wherein h_{cr}' (measured) is not larger than h_{cr} (theoretical).

4.3. Optimization Methods of Landslide Monitoring

Focusing on the plate-shaped translational landslide through the existing field monitoring result experience and deformation and failure mode exploration, this study proposes the long-term monitoring method with more parameters referring to the characteristics of such landslides.

First, long-term monitoring should be conducted to obtain sufficient monitoring data, which mainly includes obtaining groundwater level, pore-water pressure, rainfall intensity, and displacement data on the front edge of the landslide during monsoon, as well as focusing on the change of overall inclination of the plate girder during the non-rainy season. This is because the inclination angle α relative to the sliding surface also changes after the sliding of the plate girder. Thus, the inclination measuring device which consists of three-axis accelerometer and electronic compass should be installed in the sliding body, to verify the theoretical exploration of deformation mode of the plate-shaped sliding body in the non-rainy season in Fig. 13(c). Furthermore, a sensitivity analysis of various parameters affecting the stability coefficient K of the sliding body (such as the pore-water level, internal cohesive force in saturated water, internal

friction angle of the sliding surface, and inclination angle of the plate girder) should be conducted on the basis of the monitoring data. Therefore, an in-depth analysis and exploration of the deformation and failure mode of the plate-shaped landslide would be beneficial and would improve the success rate of landslide warning.

5. Conclusions

Considering the case of the Wobaoshi landslide as an example, this study uses research methods such as field exploration, a long-term monitoring engineering, geomechanical model analysis and numerical simulation to deeply analyze the instability conditions and failure characteristics of a special type of translational landslide. The research results are beneficial to the stability analysis and evaluation of this type of landslide. Targeted monitoring methods are proposed to enrich theoretical research on the translational landslide. The following conclusions are drawn:

(1) The characteristics, formation conditions, and occurrence mechanism of rainfall-triggered translational plate-shaped landslides are summarized herein. Such landslides generally exist in a consequent slope with the inclination angle of the sliding surface being less than 10° , and a group of long and straight structural planes parallel to the slope cuts the slope into several thin plates. The plate-shaped sliding body generally contains extremely thick sandstone, which is nearly horizontal and has good integrity. The bottom sliding zone is a weak mudstone interlayer affected by periodic rainfalls. In addition, single-stage or multistage plate-shaped sliding bodies slide horizontally along the bottom mudstone sliding zone.

(2) Based the mechanical model of the plate-shaped sliding bodies, the relationship between the stability coefficient of the multistage sliding body, K , and the pore-water level, h , was obtained, and the maximum pore-water level, h_{cr} , which causes the instability of multi-stage plate girders was calculated. The instability conditions of the plate-shaped sliding bodies were also determined.

(3) Theoretical conclusions of the plate-shaped landslide research were verified using the long-term monitoring data. The multiparameter monitoring data show that the stability of the sliding body is considerably affected by the rainfall intensity and pore-water pressure. The pore-water pressure in the crack is positive for the beginning of the plate-shaped sliding body, which demonstrates the rainfall-triggered failure mode of the translational landslide. This study compares and analyzes the measured maximum pore-water level h'_{cr} and theoretical calculated value h_{cr} , and discusses the influence in the change of internal cohesive force and internal friction angle on the stability coefficient of the sliding body.

(4) Combined with landslide numerical simulation, this study analyzes and explores the deformation and failure modes of the plate-shaped landslide, i.e., combined with the pore-water pressure in the crack and seepage effect in monsoon, the sliding bodies will slide horizontally along the contact surface of the bottom sand-mud rock weak layer. During the non-rainy season, the pore-water pressure decreases and disappears; the sliding body, owing to its dead weight, will be inclined to the trailing edge. On this basis, this study proposes an optimized monitoring methodology to closely monitor the pore-water pressure, rainfall, and landslide frontal displacement during monsoon, proposed method focuses on the overall inclination angle change of the plate girder during the non-rainy season.

525

526 **Acknowledgments**

527 We thank Dr. Long Chen at the Institute of Exploration Technology of CAGS for providing
528 landslide monitoring data. This work was supported by the National Natural Science Foundation
529 of China (41804089), Project of Observation Instrument Development for Integrated Geophysical
530 Field of China Mainland (Y201802), and CGS of China Geological Survey Project
531 (1212011220169 and 12120113011100).

532

533 **References**

534 Bellanova, J., Calamita, G., Giocoli, A., Luongo, R., Piscitelli, S.: Electrical resistivity imaging for the
535 characterization of the Montaguto landslide(southern Italy), Engineering Geology,
536 243(1):272-281, 2018.

537 Barlow, J., Martin, Y., Franklin, S. E.: Detecting translational landslide scars using segmentation of
538 Landsat ETM+ and DEM data in the northern Cascade Mountains, British Columbia,
539 Canadian Journal of Remote Sensing, 29(4):510-517, 2003.

540 Brown, E., Hoek, E.: Trends in relationships between measured in-situ stresses and depth. International
541 Journal of Rock Mechanics and Mining Sciences & Geomechanics Abstracts, 15(4):78-85,
542 1978.

543 Cruden, D.M., Varnes, D.J.: Landslides investigation and mitigation, Special Report 247,
544 Transportation Research Board, National Research Council [R]. [S. l.]:[s. n.], 1996.

545 Darve F., Vardoulakis I.: Degradations and Instabilities in Geomaterials, Springer Vienna, Austria,
546 2004.

547 Emelyanova E.II.: The basic rule of landslide movement, Chongqing Publishing House, Chongqing,
548 China, 1986.

549 Fan, X., Xu, Q., Zhang, Z., et al: The genetic mechanism of a translational landslide, Bulletin of
550 Engineering Geology and the Environment, 68(2):231-244, 2009.

551 Fan, X.: Mechanism and remediation measures for translational landslide [M. S. Thesis], Chengdu:
552 Chengdu University of Technology, 2007.

553 Fan X., Xu Q., Zhang Z., et al: Study of genetic mechanism of translational landslide, Chinese Journal
554 of Rock Mechanics and Engineering, 27(Supp.2):3753-3759, 2008.

555 Guzzetti, F., Cardinali, M., Reichenbach P., et al.: Landslides triggered by the 23 November 2000
556 rainfall event in the Imperia Province, Western Liguria, Italy, Engineering Geology,
557 73(3-4):229-245, 2004.

558 Guo X., Huang R., Deng H., Xu Q., ZHAI G.: Formation and mechanism analysis of multi-level rift
559 trough in translational sliding landslide, Journal of Engineering Geology, 21(5):770-778, 2013.

560 Labuz J. F., Zang A.: Mohr–Coulomb Failure Criterion, Rock Mechanics and Rock Engineering,
561 (2012)45:975–979, 2012.

562 Lin J. Yang W., Bao C.: Progressive collapse mechanism of hybrid structures with different vertical
563 stiffness, China Earthquake Engineering Journal, 40(4):713-720, 2018.

564 Liu Y., Wang J.: The research and application of landslide surface crack monitoring method based on

565 laser ranging mode, Environmental and Earth Sciences Research Journal, 2(2):19-24, 2015.

566 Chen L., Liu Y., Feng X.: The investigation report on remediation project of Wobaoshi landslide,
567 Sanhui Town, Enyang District, Bazhong City, The Institute of Exploration Technology of
568 CAGS, Chengdu, Open File Rep., pp.57, 2015.

569 Griffiths, D. V., Lane, P. A.: Slope stability analysis by finite elements, Géotechnique, 49(3), 387-403,
570 1999.

571 Martin, Y. E., Franklin, S. E.: Classification of soil- and bedrock-dominated landslides in British
572 Columbia using segmentation of satellite imagery and DEM data, International Journal of
573 Remote Sensing, 26(7):1505-1509, 2005.

574 Matjaž, M., Matja, C., Mitja, B.: Hydrologic conditions responsible for triggering the Stože landslide,
575 Slovenia, Engineering Geology, 73(3-4):193-213, 2004.

576 Mario, F., Francesca, B.: Evaluation of landslide reactivation: a modified rainfall threshold model
577 based on historical records of rainfall and landslides, Geomorphology, 94(1-2): 40-57, 2008.

578 Sergio, D. N., Lourenco, K. S., Hiroshi, F.: Failure process and hydrologic response of a two layer
579 physical model: Implications for rainfall-induced landslides, Geomorphology, 73(1-2):115-130,
580 2006.

581 Teixeira, M., Bateira, C., Marques, F., et al: Physically based shallow translational landslide
582 susceptibility analysis in Tibo catchment, NW of Portugal, Landslides, 12(3):455-468, 2015.

583 Tschuchnigg, F., Schweiger, H.F. & Sloan, et al: Slope stability analysis by means of finite element
584 limit analysis and finite element strength reduction techniques. Part I: Numerical studies

585 considering non-associated plasticity, *Computers and Geotechnics*, 70, 169-177, 2015.

586 Tschuchnigg, F., Schweiger, H.F., Sloan, S.W., et al: Comparison of finite-element limit analysis and
587 strength reduction techniques, *Géotechnique*, 65(4), 249-257, 2015.

588 Wang L., Zhang Z.: The mechanical patterns of the deformation in rock slope, Geological Publishing
589 House, Beijing, China, 1985.

590 Xu Q., Zeng Y.: Research on acceleration variation characteristics of creep landslide and early-warning
591 prediction indicator of critical sliding, *Chinese Journal of Rock Mechanics and Engineering*,
592 28(6):1099-1106, 2009.

593 Xu Q., Huang R., Liu T., et al.: Study of the formation mechanism and design of control engineering
594 for the super-huge Tiantai landslide, *IAEG2006 Engineering Geology for Tomorrow Cities*,
595 Sichuan province, China, 2006, 602.

596 Xu Q., Fan X., Li Y., Zhang S.: Formation condition, genetic mechanism and treatment measures of
597 plate-shaped landslide, *Chinese Journal of Rock Mechanics and Engineering*, 29(2):242-250,
598 2010.

599 Yin K., Jian W., Zhou C., et al: Study on the mechanism of the translational landslide in Wanzhou
600 district and prevention project, Wuhan: China University of Geosciences , Open File,
601 pp.153-154, 2005.

602 Zhang Z., Wang S., Wang L.: The analytical principle on engineering geology, Geological Publishing
603 House, Beijing, China, 1994.

604 Zhang L., Pei X., Lin H., Li S.: Evolution of Landslide Based on Growth Characteristics of Trees on

605 the Landslide, Mountain Research, 33(4):503-510, 2015.

606

Figure Captions

Fig. 1. Geographical location and elevation map of the Wobaoshi landslide.

Fig. 2. Topographic map of the Wobaoshi landslide and photographs of observation points: (a) exposed bedrock at the front edge; (b) the houses had cracked at the front edge (c) the roadbed is pushed uplifted at the front edge; (d) crack II and bent trees; and (e) crack I.

Fig. 3. I- I' sectional graph of the landslide.

Fig. 4. Layout planar graph of the monitoring equipment.

Fig. 5. Photos of installation the monitoring instruments: (a) crack I gauge; (b) rain gauge and pore-water pressure gauge; and (c) crack II gauge.

Fig. 6. Monitoring data curves (rainfall intensity and width of cracks I and II).

Fig. 7. Monitoring data curves: (a) width of crack I and its pore-water pressure; (b) width of crack II and its pore-water pressure.

Fig. 8. Absolute stretching amount curves of cracks I and II.

Fig. 9. Geomechanical model of two-stage plate-shaped sliding bodies.

Fig. 10 Determination of the maximum pore-water level h_{cr}' (measured) .

Fig. 11. Comparison figure of h_{cr}' (measured) and h_{cr} (theoretical).

Fig. 12 Example of finite element simulation and numerical calculation.

Fig. 13 Schematic of the deformation and failure mode of the Wobaoshi landslide.

Table

Table 1 Typical monitoring data of the Wobaoshi landslide

| Measurement duration | Crack I width (m) | Crack II width (m) | Crack I Pore-water pressure (kPa) | Crack II Pore-water pressure (kPa) |
|----------------------|-------------------|--------------------|-----------------------------------|------------------------------------|
| 2015/2/1 | 5.640 | 4.492 | 0 | 0 |
| 2015/4/24 | 5.945 | 4.774 | 18.561 | 27.303 |
| 2015/5/7 | 5.886 | 4.798 | 18.649 | 33.212 |
| 2015/5/13 | 6.203 | 4.810 | 33.134 | 33.036 |
| 2015/5/15 | 6.215 | 4.899 | 34.476 | 35.456 |
| 2015/8/15 | 6.350 | 5.451 | 41.474 | 31.625 |
| 2015/9/14 | 6.330 | 5.380 | 34.594 | 30.772 |
| 2015/11/15 | 5.871 | 4.952 | 11.280 | 17.395 |
| 2016/2/15 | 5.790 | 4.599 | 0 | 0 |
| 2016/4/13 | 5.824 | 4.706 | 10.378 | 26.156 |
| 2016/5/14 | 6.173 | 4.850 | 33.810 | 36.035 |
| 2016/7/17 | 6.161 | 5.281 | 36.162 | 31.664 |
| 2016/8/18 | 6.310 | 5.220 | 38.024 | 33.683 |
| 2016/9/15 | 6.325 | 5.251 | 39.298 | 29.723 |
| 2016/12/20 | 5.960 | 4.763 | 5.106 | 0 |
| 2017/2/16 | 5.865 | 4.770 | 0 | 0 |
| 2017/4/13 | 5.984 | 5.152 | 24.108 | 29.155 |
| 2017/5/17 | 6.118 | 5.332 | 43.463 | 31.703 |
| 2017/7/17 | 6.433 | 5.239 | 42.787 | 30.478 |
| 2017/8/15 | 6.490 | 5.255 | 43.639 | 29.273 |
| 2017/11/14 | 6.091 | 5.004 | 5.488 | 8.428 |
| 2017/12/20 | 5.922 | 4.723 | 0 | 0 |
| 2018/1/11 | 5.881 | 4.751 | 0 | 0 |
| 2018/4/10 | 6.194 | 5.110 | 33.957 | 35.819 |
| 2018/5/17 | 6.283 | 5.246 | 33.830 | 33.438 |
| 2018/6/16 | 6.452 | 5.315 | 36.995 | 28.391 |
| 2018/7/10 | 6.421 | 5.310 | 38.171 | 29.841 |

Table 2 Rainfall intensity value of the Wobaoshi landslide (mm/month)

| Year | Month | | | | | | | | | | | | Total |
|------|-------|------|------|------|-------|-------|-------|-------|-------|------|------|------|--------|
| | 1 | 2 | 3 | 4 | 5 | 6 | 7 | 8 | 9 | 10 | 11 | 12 | |
| 2015 | | 13.5 | 30.5 | 71.8 | 121.9 | 165.0 | 240.1 | 163.0 | 166.1 | 85.0 | 39.6 | 14.1 | 1110.6 |
| 2016 | 6.9 | 12.5 | 26.5 | 56.8 | 98.4 | 126.1 | 193.2 | 155.1 | 150.0 | 90.3 | 29.1 | 13.5 | 958.4 |
| 2017 | 5.7 | 16.8 | 36.8 | 90.5 | 115.6 | 185.1 | 271.3 | 190.0 | 176.2 | 109 | 52.1 | 20.8 | 1269.9 |
| 2018 | 11.5 | 10.9 | 31.5 | 99.9 | 121.0 | 205.1 | 191.6 | | | | | | 671.5 |

632

Table 3 Measured pore-water level data of the sliding bodies

| Measured time | Crack I slippage (m) | Measured pore-water level (m) | Crack II slippage (m) | Measured pore-water level (m) |
|---------------|-------------------------|----------------------------------|--------------------------|----------------------------------|
| 2015/4/15 | 0.072 | 14.566 | 0.183 | 12.736 |
| 2015/4/24 | 0.305 | 15.174 | 0.282 | 12.936 |
| 2015/5/7 | 0.246 | 15.183 | 0.306 | 13.539 |
| 2015/5/13 | 0.561 | 16.661 | 0.318 | 13.521 |
| 2015/5/15 | 0.573 | 16.798 | 0.407 | 13.768 |
| 2015/6/20 | 0.711 | 17.032 | 0.888 | 13.502 |
| 2015/7/17 | 0.519 | 17.474 | 0.798 | 13.471 |
| 2015/10/16 | 0.481 | 16.470 | 0.538 | 13.340 |
| 2015/11/15 | 0.229 | 14.431 | 0.458 | 11.925 |
| 2016/1/15 | 0.108 | \ | 0.169 | \ |
| 2016/4/13 | 0.184 | 13.490 | 0.214 | 12.819 |
| 2016/4/23 | 0.421 | 14.339 | 0.269 | 12.804 |
| 2016/4/29 | 0.475 | 16.214 | 0.432 | 13.835 |
| 2016/5/11 | 0.469 | 16.494 | 0.449 | 13.920 |
| 2016/5/14 | 0.531 | 16.505 | 0.358 | 13.827 |
| 2016/6/15 | 0.508 | 16.731 | 0.618 | 13.574 |
| 2016/9/15 | 0.683 | 17.312 | 0.758 | 13.183 |
| 2016/10/12 | 0.637 | 14.930 | 0.618 | 12.360 |
| 2017/2/16 | 0.223 | \ | 0.278 | \ |
| 2017/4/13 | 0.344 | 15.741 | 0.658 | 13.125 |
| 2017/4/29 | 0.489 | 16.712 | 0.686 | 13.141 |
| 2017/5/2 | 0.518 | 16.799 | 0.648 | 13.024 |
| 2017/5/13 | 0.501 | 16.877 | 0.734 | 13.161 |
| 2017/5/17 | 0.476 | 17.715 | 0.838 | 13.385 |
| 2017/8/15 | 0.848 | 17.733 | 0.758 | 13.137 |
| 2017/9/16 | 0.869 | 16.324 | 0.333 | 12.235 |
| 2018/3/14 | 0.281 | \ | 0.618 | 11.013 |
| 2018/4/10 | 0.552 | 16.745 | 0.754 | 13.805 |
| 2018/5/17 | 0.643 | 16.732 | 0.333 | 13.562 |

633

634

Table 4 Mechanical parameters of the sliding body model

| Lithology | Elastic Modulus (N/m ²) | Poisson Ratio | Gravity (N) | Internal Cohesion (N/m ²) | Internal Friction Angle | Permeability Coefficient (cm/s) |
|----------------|-------------------------------------------|------------------|-------------|---------------------------------------------|-------------------------------|---------------------------------------|
| Arkose | 600000 | 0.25 | 19200 | 30000 | 36° | 1.20E-07 |
| Silty Mudstone | 360000 | 0.28 | 19000 | 20000 | 30° | 6.00E-07 |
| Clay | 300000 | 0.3 | 18000 | 10200 | 11.2° | 1.20E-06 |

635

636

637

Table 5 Loading steps of the water level in Crack I and II in FEM model

| Loading Steps | Crack I | Crack II |
|---------------|----------|----------|
| 0 | 314.50 m | 311.00 m |
| 1 | 316.00 m | 313.00 m |
| 2 | 317.50 m | 315.00 m |
| 3 | 316.00 m | 313.00 m |
| 4 | 314.50 m | 311.00 m |

638